Physics-Based Model Predictive Control for Power Capability Estimation of Lithium-Ion Batteries

Yang Li, *Member, IEEE,* Zhongbao Wei, *Senior Member, IEEE,* Changjun Xie, *Member, IEEE,* and D. Mahinda Vilathgamuwa, *Fellow, IEEE*

***Abstract*—The power capability of a lithium-ion battery signifies its capacity to continuously supply or absorb energy within a given time period. For an electrified vehicle, knowing this information is critical to determining control strategies such as acceleration, power split, and regenerative braking. Unfortunately, such an indicator cannot be directly measured and is usually challenging to be inferred for today's high-energy type of batteries with thicker electrodes. In this work, we propose a novel physics-based battery power capability estimation method to prevent the battery from moving into harmful situations during its operation for its health and safety. The method incorporates a high-fidelity electrochemical-thermal battery model, with which not only the external limitations on current, voltage, and power, but also the internal constraints on lithium plating and thermal runaway, can be readily taken into account. The online estimation of maximum power is accomplished by formulating and solving a constrained nonlinear optimization problem. Due to the relatively high system order, high model nonlinearity, and long prediction horizon, a scheme based on multistep nonlinear model predictive control is found to be computationally affordable and accurate.**

***Index Terms*—Lithium-ion batteries, model predictive control, P2D model, physics-based model, power capability, state of power.**

I. Introduction

THE ongoing transportation electrification process across the globe relies heavily on the development of lithium-ion (Li-ion) battery systems [1]. A battery management system (BMS) is essential for ensuring the efficiency, safety, and longevity of these delicate electrochemical devices. Many fundamental functionalities must be carefully designed to monitor the internal states, and operating limits, which can provide critical signs for high-level energy management and control systems [2]. The power capability of a battery is such a useful performance indicator, which represents how much energy the battery can charge or discharge within a given time interval [3]. For example, the discharge power capability signifies the accelerating capability of an electric vehicle (EV), and the charge power capability is associated with the effectiveness of regenerative braking. When an EV is under recharging at the fast charging station or participating in vehicle-to-grid/vehicle-to-home services when parking, the power capability determines the maximum charging/discharging rate that can be reached [4]–[6]. Furthermore, for hybrid electric vehicles, knowing the power capability can be helpful in determining the power split. As the power capability is affected by various factors such as the battery state of charge (SOC), state of health (SOH), temperature, and some external operating limitations, battery manufacturers usually cannot provide exact power capability information in the specification. An accurate estimate of the power capability is essential to achieve high-performance management of the battery itself as well as the entire energy conversion system.

In the literature, the term *power capability* is also referred to as or related to state-of-power, available power, peak power, state of available power, and state of function, to name a few. Despite the variation in names and definitions, the difference in usage is trivial, and the estimation algorithms for these power indicators can be generally classified into the offline and the online methods. Offline methods, such as characteristic maps, are established based on deterministic relationships between state variables such as SOC and temperature, as well as power pulse parameters [7]. However, these static methods lack the necessary adaptation to the varying performance of cells, caused by battery aging and past and present operating conditions. In contrast, online power capability prediction/estimation techniques based on mathematical battery models have been explored and exploited more extensively. Commonly, equivalent circuit models (ECMs) are adopted in the existing works due to their simple structure and low computation [8]–[10]. The constraints that can be used to calculate the power limits include the current, voltage, SOC, and temperature. A comparative study on different ECM-based power capability estimation methods can be found in [11].

Unfortunately, the ECM-based power capability estimation is plagued by the requirements of accurate parameter identification for extreme conditions close to the constraint boundary. Usually, circuit parameters are considered as a function of SOC and temperature, and simple recursive algorithms can be used to estimate the circuit parameters during online operation [12]. However, as an electrochemical device, a battery is a highly nonlinear and infinite-dimensional system, and the circuit parameters can also be affected by many other factors such as current magnitude and frequency [13]. Since current or power is the quantity to be estimated, usually with large magnitudes, it is less reasonable to use the parameter-

This work was supported in part by National Key R&D Project of China under Grant 2022YFB2405700, in part by the National Natural Science Foundation of China under Grant 51977164, and in part by Horizon 2020 Marie Skłodowska-Curie Actions Individual Fellowships under Grant 895337.

Yang Li is with the Department of Electrical Engineering, Chalmers University of Technology, 41296 Gothenburg, Sweden (e-mail: yangli@ieee.org)

Zhongbao Wei is with the School of Mechanical Engineering, Beijing Institute of Technology, Beijing 100081, China (e-mail: weizb@bit.edu.cn).

Changjun Xie is with the School of Automation, Wuhan University of Technology, Wuhan 430070, China (e-mail: jackxie@whut.edu.cn).

D. Mahinda Vilathgamuwa is with the School of Electrical Engineering and Robotics, Queensland University of Technology, Brisbane, QLD 4001, Australia (e-mail: mahinda.vilathgamuwa@qut.edu.au).

s identified under a different operating condition. In other words, apart from the bulk indicators such as SOC, SOH, and lumped cell temperature, the power capability is also closely related to the nonuniform behaviors of internal states, while the generalization capability of the conventional lumped-parameter ECM can be poor unless high-order ECMs and high-dimensional lookup tables are adopted to characterize the RC components at various operating conditions. Nevertheless, due to the empirical nature of conventional ECMs, even significantly increased experiments and model complexity do not guarantee that accurate results can be obtained under extreme conditions where data are not covered. Extrapolation of the degradation behaviors and prediction of safety margin inside of the cell using ECMs is also prone to fail due to the lack of mechanistic description of related behaviors, e.g., the growth of the solid-electrolyte interphase film, Li plating, and thermal runaway.

Instead, one can use a physics-based model (PBM) to solve the problems of empirical ECMs due to its high extrapolability and the capability to predict the internal behaviors related to battery health and safety. One of the most widely adopted PBMs, namely the pseudo-two-dimensional (P2D) model, can be used to describe various electrochemical phenomena, such as ion diffusion, intercalation kinetics, as well as heat generation/heat transfer. Such a model is capable of reproducing battery dynamics and accurately predicting the internal operating limits with high fidelity [14]. Since the P2D model consists of coupled partial differential-algebraic equations (PDAEs), model order reduction is commonly needed for designing and implementing online model-based algorithms [1]. The most widely investigated reduced-order model (ROM) is the isothermal single particle model (SPM), which describes the diffusion of each electrode in a lumped spherical particle and ignores the influences of electrolyte dynamics and heat transfer. However, its capability to predict battery performance is only limited to low to medium current rates. The accuracy of the SPM can be first improved by adding back the electrolyte dynamics as considered in the P2D model, and further enhanced by incorporating a certain thermal model [15]. Although the single-particle-based model has been adopted in the literature for advanced power capability prediction [16], the uniform assumption for each electrode holds only for very thin electrodes or under low to medium current rates, but can be significantly violated in other conditions, especially for the future high-energy battery cells with ever-thicker electrodes [17]. Furthermore, the extended operating range can lead to significant nonuniform degradation behaviors in the electrode. For example, degradation behaviors such as Li plating can develop nonuniformly over the negative electrode and is observed to occur most significantly at the separator-anode interface [18]. Clearly, the lumped electrode in the single-particle-based models does not comply with the operating conditions under which the power capability is calculated.

The recent technological advancements in modern microprocessors and cloud computing unlock the possibility of using high-fidelity models for battery state estimation and control purposes in advanced BMS. This fact motivates us in this work to develop novel physics-based power capability estimation algorithms to close the gap as mentioned above, and to overcome the problems of existing power capability estimation algorithms based on offline, lumped-parameter ECMs, or electrochemical SPM-based algorithms. Specifically, in contrast, a computationally affordable physics-based circuit model is adopted to design model predictive control (MPC) strategies to predict the maximum battery power. The major advantages of the proposed methods over the existing power capability estimation methods are the ameliorated generality and extrapolability to wide operating regimes and the potential to include the internal health and safety constraints to avoid critical issues, including Li plating and thermal runaway. To our best knowledge, this is the first attempt to use high-fidelity physics-based models with nonuniform porous electrodes for Li-ion battery power capability estimation.

II. Physics-Based Modeling of Li-Ion Batteries

As mentioned in the introduction section, a PBM can provide much more insight into the internal operating limits apart from the external constraints under extended operating ranges for power capability prediction. In this section, we provide an overview of a high-fidelity PBM of Li-ion batteries for the development of the power capability estimation algorithm in the latter sections.

The P2D model of Li-ion batteries is a PDAE system established using the porous electrode theory and the concentrated solution theory [14]. Three physical compartments, including the positive electrode (i.e., the cathode, denoted by "pos"), the negative electrode (i.e., the anode, denoted by "neg"), and the separator (sep), are modeled within three mathematical domains. The submodels of the P2D model describe the diffusion and migration of Li species in different domains. The transmission-line-like circuit network in Fig. 1 can be used to illustrate the model structure. This network can be obtained by applying the finite volume method (FVM) to the partial differential equations (PDEs) that describe the charge transport along the horizontal direction. The domains of the positive electrode, separator, and negative electrode are divided into N^{pos}, N^{sep}, and N^{neg} control volumes, respectively. The subscript $i \in \{1, 2, \cdots, N^{\text{tot}}\}$ indicates the local quantities at the ith control volume, where $N^{\text{tot}} = N^{\text{pos}} + N^{\text{sep}} + N^{\text{neg}}$ is the total number of control volumes. This spatially discretized model will be briefly explained next. For the ease of notation, we define the following index sets of control volumes $\mathcal{I}^{\text{pos}} := \{1, 2, \cdots, N^{\text{pos}}\}$, $\mathcal{I}^{\text{sep}} := \{N^{\text{pos}}+1, \cdots, N^{\text{pos}}+N^{\text{sep}}\}$, and $\mathcal{I}^{\text{neg}} := \{N^{\text{pos}} + N^{\text{sep}} + 1, \cdots, N^{\text{tot}}\}$. Furthermore, we use superscripts such as "neg/sep" and "pos/sep" to indicate the control volume at an electrode/separate boundary, and use "neg/col" and "pos/col" to indicate the control volume at an electrode/current collector boundary, as indicated in Fig. 1.

In Fig. 1, $U_{\text{ss},i}$ and $U_{e,i}$ are concentration- and temperature-controlled voltage sources, denoted by

$$U_{\text{ss},i} = f_{\text{ss},i}(c_{\text{ss},i}, T_{\text{bat}}), \quad i \in \mathcal{I}^{\text{pos}} \cup \mathcal{I}^{\text{neg}} \tag{1}$$

$$U_{e,i} = f_{e,i}(c_{e,i}, T_{\text{bat}}), \quad i \in \mathcal{I}^{\text{pos}} \cup \mathcal{I}^{\text{sep}} \cup \mathcal{I}^{\text{neg}} \tag{2}$$

where $c_{\text{ss},i}$, $c_{e,i}$, and T_{bat} are the local solid-phase surface concentration, local electrolyte concentration, and lumped battery temperature, respectively. $f_{\text{ss},i}(\cdot)$ and $f_{e,i}(\cdot)$ are nonlinear

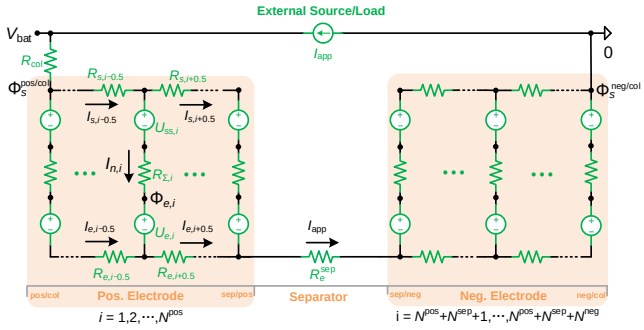

Fig. 1. Equivalent circuit representation of PBM of a Li-ion battery cell with thick electrodes.

functions determined by the material characteristics of the electrodes and the electrolyte material, respectively.

According to the equivalent circuit network in Fig. 1, given the input current I_{app} and considering that the voltage sources $U_{\text{ss},i}$ and $U_{e,i}$ are only state-dependent, one can solve for all branch currents including $I_{n,i}$, $I_{e,i\pm0.5}$, and $I_{s,i\pm0.5}$. For example, the solution of $I_{n,i}$ (which is proportional to the local pore-wall molar flux $j_{n,i}$) in the positive electrode can be vectorized as,

$$\mathbf{I}_n^{\text{pos}} = \mathbf{K}_{n,\text{ZSR}}^{\text{pos}} I_{\text{app}} + \mathbf{G}_{n,\text{ZIR}}^{\text{pos}} (\mathbf{U}_{\text{ss}}^{\text{pos}} + \mathbf{U}_e^{\text{pos}}) \tag{3}$$

where $\mathbf{I}_n^{\text{pos}}$, $\mathbf{U}_{\text{ss}}^{\text{pos}}$, and $\mathbf{U}_e^{\text{pos}}$ are vectors that contain $I_{n,i}$, $U_{\text{ss},i}$, and $U_{e,i}$, respectively, where $i \in \mathcal{I}^{\text{pos}}$. In the circuit theory, the two terms on the RHS of (3) are the zero-state response (ZSR) and zero-input response (ZIR) components of $\mathbf{I}_n^{\text{pos}}$, respectively. For the negative electrode, A similar result can be obtained, i.e.,

$$\mathbf{I}_n^{\text{neg}} = \mathbf{K}_{n,\text{ZSR}}^{\text{neg}} I_{\text{app}} + \mathbf{G}_{n,\text{ZIR}}^{\text{neg}} (\mathbf{U}_{\text{ss}}^{\text{neg}} + \mathbf{U}_e^{\text{neg}}) \tag{4}$$

Here, the vectors $\mathbf{K}_{n,\text{ZSR}}^{\text{pos}}$, $\mathbf{K}_{n,\text{ZSR}}^{\text{neg}}$ and the square matrices $\mathbf{G}_{n,\text{ZIR}}^{\text{pos}}$, $\mathbf{G}_{n,\text{ZIR}}^{\text{neg}}$ are determined by the resistances in the respective electrodes as shown in Fig. 1 and the reader is referred to Eqs. (C.3) and (C.4) of [14] for their detailed expressions.

The local concentrations $c_{\text{ss},i}$ and $c_{e,i}$, and battery SOC are governed by reduced diffusion equations that can be generally expressed by

$$\dot{\mathbf{x}}_c = \mathbf{A}_c \mathbf{x}_c + \mathbf{B}_c \begin{bmatrix} \mathbf{I}_n^{\text{pos}} \\ \mathbf{I}_n^{\text{neg}} \end{bmatrix} \tag{5}$$

$$[\mathbf{c}_{\text{ss}}^\top, \mathbf{c}_e^\top, c_{s,\text{avg}}^{\text{neg}}]^\top = \mathbf{C}_c \mathbf{x}_c \tag{6}$$

$$\text{SOC} = \frac{c_{s,\text{avg}}^{\text{neg}} - c_{s,0\%}^{\text{neg}}}{c_{s,100\%}^{\text{neg}} - c_{s,0\%}^{\text{neg}}} \tag{7}$$

where $\mathbf{x}_c$ is a vector containing all concentration states, $\mathbf{c}_{\text{ss}}$ is a vector containing all $c_{\text{ss},i}$, $\mathbf{c}_e$ contains all $c_{e,i}$, and $c_{s,\text{avg}}^{\text{neg}}$ is the bulk concentration of Li species averaged over the negative electrode volume. $c_{s,100\%}^{\text{neg}}$ and $c_{s,0\%}^{\text{neg}}$ are the solid-phase concentrations corresponding to the fully charged and fully discharged states, respectively. The matrices $\mathbf{A}_c$, $\mathbf{B}_c$, and $\mathbf{C}_c$ are determined by the model reduction method and diffusion-related parameters. The specific methods we used in this work are described in Section A of Appendix.

In addition, the battery temperature T_{bat} is described by a lumped heat transfer model,

$$C_T \dot{T}_{\text{bat}} = -(T_{\text{bat}} - T_{\text{amb}})/R_T + Q_T \tag{8}$$

where C_T is the thermal capacitance, R_T is the thermal resistance, T_{amb} is the ambient temperature. The heat generation term Q_T is considered as the sum of the power loss from all the elements in the equivalent circuit in Fig. 1. Note that this lumped thermal model is used for demonstrative purposes without the need to consider the cell's geometrical properties, while more advanced thermal models (e.g., [19]) can be incorporated into the current framework.

Since all the nodal voltage including the solid phase potential $\Phi_{s,i}$ can be obtained once (3) and (4) are solved, the battery voltage can be readily calculated by

$$V_{\text{bat}} = \Phi_s^{\text{pos/col}} - \Phi_s^{\text{neg/col}} + R_{\text{col}} I_{\text{app}} \tag{9}$$

where R_{col} is the lumped resistance of the current collectors.

Next, the local Li plating is determined by the following side-reaction potential

$$\eta_{\text{LiP},i} = U_{\text{ss},i} + R_{\Sigma,i} I_{n,i}. \tag{10}$$

The reader is referred to works such as [14], [20] for detailed information on the PBM, denoted by the P2D-T in the rest of this work.

III. Problem Formulation

A. Model Discretization and Reformulation

The P2D-T model presented in the previous section is a stiff system of nonlinear ordinary differential equations (ODEs). To improve the numerical stability, we discretize the ODEs in the time domain using an implicit-explicit (IMEX) method as described in Section B of Appendix. This yields a state transition equation in the form of

$$\mathbf{x}(k+1) = f(\mathbf{x}(k), u(k)) \tag{11}$$

where $k \in \{0, 1, \cdots\}$ is the discrete-time instant, $f : \mathbb{R}^{n_x} \times \mathbb{R} \to \mathbb{R}^{n_x}$ is a nonlinear map. The system state vector $\mathbf{x}$ of the PBM consists of concentration states and temperature, i.e., $\mathbf{x} = [\mathbf{x}_c^\top, T_{\text{bat}}]^\top \in \mathbb{R}^{n_x}$. The battery current $u = I_{\text{app}}$ is the single input of the system.

The output of the model contains all variables that can limit the battery's power capability. We divide the output variables into two groups. First, $\mathbf{y}_1$ is used to represent the output variables that are directly affected by the input u, such as the voltage V_{bat} and battery power $P_{\text{bat}} = V_{\text{bat}} I_{\text{app}}$, governed by

$$\mathbf{y}_1(k) = g_1(\mathbf{x}(k), u(k)). \tag{12}$$

Note that the model input, i.e., the battery current I_{app}, is also considered as an element of $\mathbf{y}_1$. On the other hand, we use $\mathbf{y}_2$ to denote the variables not directly affected by u but only dependent on the state $\mathbf{x}$. These variables, including SOC, concentrations, and temperature, are governed by

$$\mathbf{y}_2(k) = g_2(\mathbf{x}(k)). \tag{13}$$

To consider the influence of u on $\mathbf{y}_2$, we propagate the model (11) to yield one-step forward time-shift,

$$\mathbf{y}_2(k+1) = g_2(\mathbf{x}(k+1)) = g_2(f(\mathbf{x}(k), u(k))). \tag{14}$$

Next, we define a generalized output as

$$\mathbf{y}(k) = g(\mathbf{x}(k), u(k)) \tag{15}$$

where

$$\mathbf{y}(k) := \begin{bmatrix} \mathbf{y}_1(k) \\ \mathbf{y}_2(k+1) \end{bmatrix}, g(\mathbf{x}(k), u(k)) := \begin{bmatrix} g_1(\mathbf{x}(k), u(k)) \\ g_2(f(\mathbf{x}(k), u(k))) \end{bmatrix}.$$

By expressing the output as (15), one can simplify the analysis and implementation of the MPC-based power capability prediction algorithm, as will be explained in detail next.

B. General Problem Statement

The power capability of a battery is defined as the maximum continuous charge or discharge power under which the internal and external operating constraints are not violated over a time horizon $\tau_{\mathcal{J}}$ (e.g., $10-30$ s). The power capability is obtained by solving Problem 1.

Problem 1: At instant k, given the state estimate $\mathbf{x}(0|k) = \hat{\mathbf{x}}(k)$, we seek the optimized present and future input sequence

$$\mathbf{u}^{\star}_{\pm}(k) = \arg\max_{\mathbf{u}(k)} (\pm P_{\text{bat}}(0|k)) \tag{16a}$$

$$\text{s.t.} \quad \mathbf{x}(j+1|k) = f(\mathbf{x}(j|k), u(j|k)), \tag{16b}$$

$$\mathbf{y}(j|k) = g(\mathbf{x}(j|k), u(j|k)), \tag{16c}$$

$$P_{\text{bat}}(0|k) = P_{\text{bat}}(1|k) = \cdots P_{\text{bat}}(N_{\mathcal{J}}-1|k), \tag{16d}$$

$$\mathbf{y}(j|k) \preceq \overline{\mathbf{y}} \subset \mathbb{R}^{n_y}, \tag{16e}$$

with respect to $\mathbf{u}(k) := [u(0|k), u(1|k), \cdots, u(N_{\mathcal{J}}-1|k)]^{\top}$. The argument $j|k$ denotes the predicted quantity at the time instant $k+j$, $j \in \mathcal{J} := \{0, 1, \cdots, N_{\mathcal{J}}-1\}$ represents the distance from the predicted time instant to the present time instant k, and $N_{\mathcal{J}} = \tau_{\mathcal{J}}/\Delta t$ is the prediction horizon. The equality constraint (16d) ensures the power in the prediction horizon remains constant to meet the strict definition of the power capability. The symbol $\pm$ is "+" when evaluating the *charge power capability* $P^{\text{chg}}_{\text{max}}(k)$, while it becomes "−" for evaluating the *discharge power capability* $P^{\text{dch}}_{\text{max}}(k)$. It can be seen that by defining the general output $\mathbf{y}$ (15), the formulation of the power capability estimation problem can readily cover the terminal constraints for $\mathbf{y}_2(N_{\mathcal{J}})$. The constraints on input and state are incorporated into the general output constraints in (16e). The battery model (16a), (16b), and the inequality constraints (16e) will be discussed in the subsequent subsection.

C. Limiting Factors of Battery Power Capability

Many health and safety factors can limit the power capability for Li-ion batteries in practice. Conventionally, only the terminal conditions including battery current I_{app}, voltage V_{bat}, and power rating P_{bat} are considered, i.e.,

$$\underline{I}_{\text{app}} \le I_{\text{app}}(j|k) \le \overline{I}_{\text{app}} \tag{17a}$$

$$\underline{V}_{\text{bat}} \le V_{\text{bat}}(j|k) \le \overline{V}_{\text{bat}} \tag{17b}$$

$$\underline{P}_{\text{bat}} \le P_{\text{bat}}(j|k) \le \overline{P}_{\text{bat}}. \tag{17c}$$

Due to the limited diffusivities, the concentrations in both the solid phase and the electrolyte can show significant nonuniformity. The charge power capability is usually limited by the graphite-based negative electrode. During the charging process, the solid-phase concentration tends to saturate first at the neg/sep boundary, while the electrolyte concentration at the neg/col boundary tends to deplete first. To avoid bulk and local overcharge/overdischarge phenomenon as well as the depletion of lithium ions in the electrolyte, it is required to enforce the boundary constraints:

$$\underline{\text{SOC}} < \text{SOC}(j+1|k) \le \overline{\text{SOC}} \tag{17d}$$

$$\underline{c}^{\text{neg}}_s \le c^{\text{neg/sep}}_{\text{ss}}(j+1|k) \le \overline{c}^{\text{neg}}_s \tag{17e}$$

$$\underline{c}^{\text{neg}}_s \le c^{\text{neg/col}}_{\text{ss}}(j+1|k) \le \overline{c}^{\text{neg}}_s \tag{17f}$$

$$c^{\text{neg/col}}_e(j+1|k) \ge \underline{c}_e \tag{17g}$$

$$c^{\text{pos/col}}_e(j+1|k) \ge \underline{c}_e. \tag{17h}$$

Next, to avoid Li plating, the Li plating potential at the neg/sep boundary should be regulated above zero, i.e.,

$$\eta^{\text{neg/sep}}_{\text{LiP}}(j|k) \ge \underline{\eta}_{\text{LiP}} \ge 0. \tag{17i}$$

Last, high current flowing through the resistive components as well as electrochemical reactions can produce a large amount of heat, and heat accumulation can cause safety issues such as thermal runaway and health issues leading to accelerated aging. Assuming $\overline{T}_{\text{bat}}$ is the maximum temperature limit for health and safe operation, we have

$$T_{\text{bat}}(j+1|k) \le \overline{T}_{\text{bat}}. \tag{17j}$$

Note that either the upper or the lower constraints will be activated for the charging and discharging processes. In summary, for the charging process, the output vector is $\mathbf{y} = [I_{\text{app}}, V_{\text{bat}}, P_{\text{bat}}, \text{SOC}, c^{\text{neg/sep}}_{\text{ss}}, -c^{\text{neg/col}}_e, -\eta^{\text{neg/sep}}_{\text{LiP}}, T_{\text{bat}}]^{\top}$. The corresponding bound vector of the output is $\overline{\mathbf{y}} = [\overline{I}_{\text{app}}, \overline{V}_{\text{bat}}, \overline{P}_{\text{bat}}, \overline{\text{SOC}}, \overline{c}^{\text{neg}}_s, -\underline{c}_e, -\underline{\eta}_{\text{LiP}}, \overline{T}_{\text{bat}}]^{\top}$. On the other hand, for the discharging process, we have $\mathbf{y} = [-I_{\text{app}}, -V_{\text{bat}}, -P_{\text{bat}}, -\text{SOC}, -c^{\text{neg/col}}_{\text{ss}}, -c^{\text{pos/col}}_e, T_{\text{bat}}]^{\top}$ and $\overline{\mathbf{y}} = [-\underline{I}_{\text{app}}, -\underline{V}_{\text{bat}}, -\underline{P}_{\text{bat}}, -\underline{\text{SOC}}, -\underline{c}^{\text{neg}}_s, -\underline{c}_e, \overline{T}_{\text{bat}}]^{\top}$.

IV. Power Capability Estimation Based on Multistep Nonlinear Model Prediction Control

A. Offline and Online Solutions

The most direct approach to solve (16) is to use a global optimization technique, such as dynamic programming, or a metaheuristic method, such as the genetic algorithm. However, in a typical BMS, the optimization horizon (pulse width) $\tau_{\mathcal{J}}$ can be long as 10 to 30 s, or even longer, while the sampling time Δt is much shorter, e.g., 1 s. The long optimization horizon requires intractable computation for online operation due to the present high-order and highly nonlinear system.

There are several pathways to solve the above problem. First, model order reduction can be used to simplify the system. Although there is a vast body of model order reduction techniques for the battery models, see, e.g., [1], most of the techniques rely on the assumptions that the battery is under normal operating conditions: away from the bounds, low-to-medium current rates, normal temperature ranges, uniform

concentration distribution, etc. As for the power capability estimation, the battery is to be pushed toward the operating limits under some extreme conditions, and the underlying assumptions for most model reduction techniques become invalid. Hence, the FVM is used since it is a generic discretization technique that does not need any assumptions. The system order is not limited but subject to the requirement of model accuracy. Furthermore, the FVM preserves several physical properties, such as mass conservation, which is important for advanced battery management [21].

The second category of approaches is to use a real-time optimization method such as MPC to obtain an approximate solution. The nonlinear MPC (NMPC) is an effective method to obtain an approximate solution to global optimization. However, NMPC is subject to high computational costs and is thus considered intractable for real-time implementation of the present high-order system. The linear time-varying MPC (LTV-MPC) can be used to combat the computational problem of the NMPC, but it is not suitable for highly nonlinear systems with a long prediction horizon. This motivates us to develop a new scheme to overcome the problems of NMPC- and LTV-MPC-based schemes for the challenging task of power capability estimation.

B. NMPC-Based Power Capability Prediction

A multistep NMPC-based method is proposed as follows: At instant k, we repeatedly seek the optimizing input *subsequence* over a reduced, receding horizon $N_{\mathcal{L}} < N_{\mathcal{J}}$ given the initial state $\mathbf{x}(0|l|k)$,

$$\mathbf{u}^{\star}_{\pm}(l,k) = \arg\max_{\mathbf{u}(l,k)} [\pm P_{\text{avg}}(l,k)] \tag{18}$$

where $\mathbf{u}(l,k) := [u(0|l|k), u(1|l|k), \cdots, u(N_{\mathcal{L}}-1|l|k)]^{\top} \in \mathbb{R}^{N_{\mathcal{L}}}$ and

$$P_{\text{avg}}(l,k) = \frac{1}{N_{\mathcal{L}}} \sum_{j=0}^{N_{\mathcal{L}}-1} P_{\text{bat}}(j|l|k). \tag{19}$$

Here, $N_{\mathcal{L}}$ is denoted as the prediction horizon. Note that instead of placing an equality constraint on instantaneous battery power as in (16d), we relax the objective to maximize or minimize the average power over each prediction horizon. Such a simpler optimization problem can be solved as a constrained nonlinear programming problem with a finite time horizon. Once $\mathbf{u}^{\star}_{\pm}(l,k)$ is obtained, only the first H elements are used for forwarding the battery model and obtaining the initial state $\mathbf{x}(0|l+H|k)$ for the next optimization. Here H is denoted as the control horizon. The above optimization problem is repeatedly solved for $l \in \{0, H, 2H, \cdots (N_O-1)H\}$ to construct the final input sequence for instant k, i.e.,

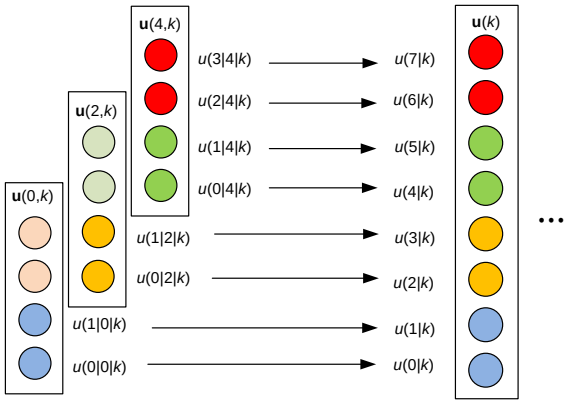

Fig. 2. Schematic of the multistep MPC based algorithm for power capability estimation with $N_{\mathcal{J}} = 8$, $N_{\mathcal{L}} = 4$, $H = 2$, and $N_O = 3$.

$$\mathbf{u}^{\star}_{\pm}(k) := \begin{bmatrix} u^{\star}(0|0|k) \\ u^{\star}(1|0|k) \\ \vdots \\ u^{\star}(H-1|0|k) \\ u^{\star}(0|H|k) \\ u^{\star}(1|H|k) \\ \vdots \\ u^{\star}(H-1|H|k) \\ \vdots \\ u^{\star}(0|(N_O-2)H|k) \\ \vdots \\ u^{\star}(H-1|(N_O-2)H|k) \\ \mathbf{u}^{\star}((N_O-1)H,k) \end{bmatrix} \tag{20}$$

where N_O is the number of optimization problems that need to be solved successively per pulse, calculated by

$$N_O = \lceil (N_{\mathcal{J}} - N_{\mathcal{L}})/H \rceil + 1 \tag{21}$$

and $\lceil \cdot \rceil$ represents the ceiling function, i.e., the least integer greater than or equal to the input. Note that when solving for (20), the corresponding power sequence, denoted by $\mathbf{P}^{\star}_{\pm}(k)$, has also been calculated. The power capability is determined by the last component in $\mathbf{P}^{\star}_{\pm}(k)$, i.e.,

$$P^{\text{chg}}_{\max}(k) = \mathbf{P}^{\star}_{+}(k + N_{\mathcal{J}} - 1) \tag{22}$$

$$P^{\text{dch}}_{\max}(k) = \mathbf{P}^{\star}_{-}(k + N_{\mathcal{J}} - 1) \tag{23}$$

Similarly, the last component in $\mathbf{u}^{\star}_{\pm}(k)$ denotes the current capability $I^{\text{chg}}_{\max}(k)$ and $I^{\text{dch}}_{\max}(k)$. To further reduce the computational burden, a commonly adopted technique can be used to impose

$$u^{\star}(0|l|k) = u^{\star}(1|l|k) =, \cdots, = u^{\star}(H-1|l|k), \tag{24}$$

so that the number of decision variables can be further reduced approximately by a factor of H.

With (24), the proposed method to construct $\mathbf{u}^{\star}(k)$ at instant k is illustrated in Fig. 2 with $N_{\mathcal{J}} = 8$, $N_{\mathcal{L}} = 4$, $H = 2$, and $N_O = 3$. The algorithm is summarized as Algorithm 1.

Algorithm 1 Multistep NMPC-Based Power Capability Estimation

Give an initial guess of the state $\hat{\mathbf{x}}(0)$.
while k **do**
  Estimate the state $\hat{\mathbf{x}}(k)$.
  $\mathbf{x}(0|k) \leftarrow \hat{\mathbf{x}}(k)$.
  for $l = 0 : H : (N_O - 1)H$ **do**
    $\mathbf{x}(0|l|k) \leftarrow \mathbf{x}(l|k)$.
    Solve (18) to obtain a sequence $\mathbf{u}^\star(l,k) \in \mathbb{R}^{N_\mathcal{L}}$ with (Algorithm 1.1) or without (24) (Algorithm 1.2).
    if $l < (N_O - 1)H$ **then**
      $u^\star(l|k) \leftarrow u^\star(0|l|k)$.
      $u^\star(l+1|k) \leftarrow u^\star(1|l|k)$.
      $\vdots$
      $u^\star(l+H-1|k) \leftarrow u^\star(H-1|l|k)$.
      Forward the physics-based battery model using $u^\star(l|k), \cdots, u^\star(l+H-1|k)$ to obtain the end-time state $\mathbf{x}(l+H|k)$.
    else if $l = (N_O - 1)H$ **then**
      for $n = 1 : N_\mathcal{J} - H(N_O - 1)$ **do**
        $u^\star(n+l|k) \leftarrow u^\star(n|l|k)$.
      end for
    end if
    Obtain the power capability $P_{\text{max}}^{\text{chg}}(k)$ using (22) and $P_{\text{max}}^{\text{dch}}(k)$ using (23).
  end for
end while

C. Ensemble-Based State Estimator for High-Dimensional Systems

Note that the state variable $\mathbf{x}(k)$ should be estimated as the initial condition for solving the MPC problem. Since the state variables of the present battery model are all unmeasurable, a state observer shall be designed to estimate them based on the battery model and measurements. Due to the presence of model uncertainty, measurements errors, and the high-dimensional nature of the battery model, an ensemble-based state estimator, such as the ensemble Kalman filter (EnKF) [20] or the singular evolutive interpolated Kalman filter [21] can be used in this framework. These ensemble-based state estimation algorithms are much less computationally demanded than conventional nonlinear observers, such as the extended Kalman filter and the unscented Kalman filter that have been widely adopted in the battery management community.

As an example, the EnKF is adopted in this work, initialized by choosing a proper initial state ensemble $\hat{\mathbf{X}}(0|0) := [\hat{\mathbf{x}}^{(1)}(0|0), \hat{\mathbf{x}}^{(2)}(0|0), \cdots, \hat{\mathbf{x}}^{(N_\mathcal{P})}(0|0)]$ where $N_\mathcal{P}$ is the ensemble size. The prior state ensemble $\hat{\mathbf{X}}(k|k-1) := [\hat{\mathbf{x}}^{(1)}(k|k-1), \hat{\mathbf{x}}^{(2)}(k|k-1), \cdots, \hat{\mathbf{x}}^{(N_\mathcal{P})}(k|k-1)]$ is obtained according to the state equation, i.e.,

$$\begin{aligned}\hat{\mathbf{x}}^{(p)}(k|k-1) =& f(\hat{\mathbf{x}}^{(p)}(k-1|k-1), u(k)) \\ &+ \mathbf{w}^{(p)}(k) \quad \forall p \in \mathcal{P}. \end{aligned} \tag{25}$$

where $\mathcal{P} := \{1, 2, \cdots, N_\mathcal{P}\}$.

To assimilate the latest measurements $z(k) = V_{\text{bat}}(k)$ to obtain the posterior state ensemble $\hat{\mathbf{X}}(k|k) := [\hat{\mathbf{x}}^{(1)}(k|k), \hat{\mathbf{x}}^{(2)}(k|k), \cdots, \hat{\mathbf{x}}^{(N_\mathcal{P})}(k|k)]$, a measurement ensemble $\hat{\mathbf{Z}}(k) := [\hat{z}^{(1)}(k), \hat{z}^{(2)}(k), \cdots, \hat{z}^{(N_\mathcal{P})}(k)]$ is generated, where

$$\hat{z}^{(p)}(k) = h(\hat{\mathbf{x}}^{(p)}(k|k-1), u(k)) \quad \forall p \in \mathcal{P} \tag{26}$$

The member of the posterior state ensemble $\hat{\mathbf{X}}(k|k)$ in the EnKF is updated via

$$\begin{aligned}\hat{\mathbf{x}}^{(p)}(k|k) =& \hat{\mathbf{x}}^{(p)}(k|k-1) \\ &+ \mathbf{K}(k)(z(k) + v^{(p)}(k) - \hat{z}^{(p)}(k)) \quad \forall p \in \mathcal{P} \end{aligned} \tag{27}$$

where $v^{(p)}(k) \sim \mathcal{N}(\mathbf{0}, \mathbf{R}(k))$ is the pseudo measurement perturbation added to obtain the correct error covariance. $\mathbf{K}(k)$ is the ensemble Kalman gain expressed by

$$\mathbf{K}(k) = \frac{\tilde{\mathbf{X}}(k|k-1)\tilde{\mathbf{Z}}(k)^\top}{N_\mathcal{P} - 1} \left(\frac{\tilde{\mathbf{Z}}(k)\tilde{\mathbf{Z}}(k)^\top}{N_\mathcal{P} - 1} + \mathbf{R}(k) \right)^{-1} \tag{28}$$

Here, $\tilde{\mathbf{X}}(k|k-1) = [\tilde{\mathbf{x}}^{(1)}(k|k-1), \cdots, \tilde{\mathbf{x}}^{(N_\mathcal{P})}(k|k-1)]$ is the perturbation part of $\hat{\mathbf{X}}(k|k-1)$, where

$$\tilde{\mathbf{x}}^{(p)}(k|k-1) = \hat{\mathbf{x}}^{(p)}(k|k-1) - \frac{1}{N_\mathcal{P}} \sum_{p=1}^{N_\mathcal{P}} \hat{\mathbf{x}}^{(p)}(k|k-1) \tag{29}$$

Similarly, $\tilde{\mathbf{Z}}(k) := [\tilde{z}^{(1)}(k), \cdots, \tilde{z}^{(N_\mathcal{P})}(k)]$ is the perturbation part of $\hat{\mathbf{Z}}(k)$, where

$$\tilde{z}^{(p)}(k) = \hat{z}^{(p)}(k) - \frac{1}{N_\mathcal{P}} \sum_{p=1}^{N_\mathcal{P}} \hat{z}^{(p)}(k) \tag{30}$$

Finally, the estimate of the system state at time instant k is considered as the ensemble mean of $\hat{\mathbf{X}}(k|k)$, i.e.,

$$\hat{\mathbf{x}}(k) = \frac{1}{N_\mathcal{P}} \sum_{p=1}^{N_\mathcal{P}} \hat{\mathbf{x}}^{(p)}(k|k) \tag{31}$$

V. Illustrative Examples

A. System Configuration

In this section, the proposed battery power capability estimation strategy is numerically examined. Both the plant and the control were simulated in MATLAB R2019b on a PC with a processor of Intel Core i7 and RAM of 16 GHz. The fidelity of the presented P2D-T model has been validated in various existing works. For parameterizing a Li-ion battery, the general steps are briefly described as follows. First, the function of the open-circuit potential (OCP) of the negative electrode (i.e., $f_{\text{ss},i}(\cdot), i \in \mathcal{I}^{\text{neg}}$ in (1)) was obtained from the literature, and the OCP function of the positive electrode was fitted as the sum of measured open-circuit voltage and the OCP of the negative electrode. Sensitivity analysis was next conducted based on the measurements. Most of the material-dependent parameters and the parameters with low sensitivities to input were obtained from the literature, and the remaining parameters were identified using the genetic algorithm. In this work, the model parameters are for a 5-Ah NMC811/graphite-silicon battery cell and provided in Table II and Table III in Section A of Appendix.

The ODE plant model (1)–(10) was solved using `ode32tb` function and the numbers of control volumes were selected as

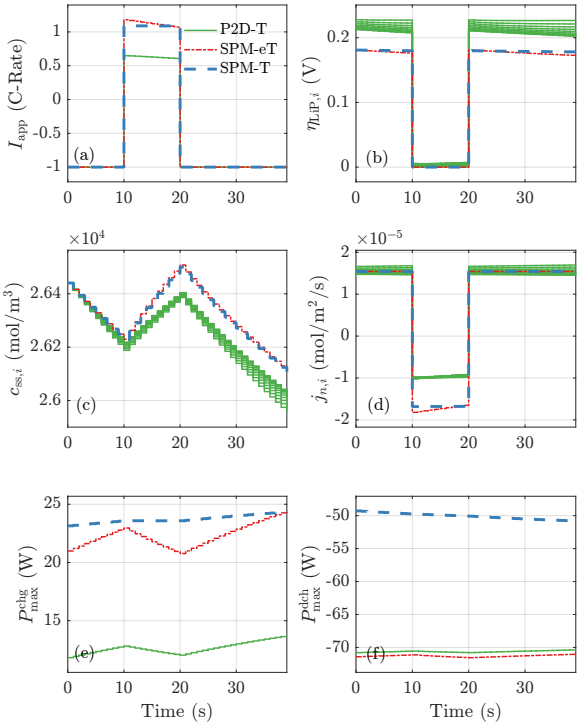

Fig. 3. Model comparison for battery power capability estimation. (a) Applied current rate. (b) Li plating potential in the negative electrode. (c) Solid-phase surface concentration in the negative electrode. (d) Pore-wall molar flux in the negative electrode. (e) Charge power capability. (f) Discharge power capability.

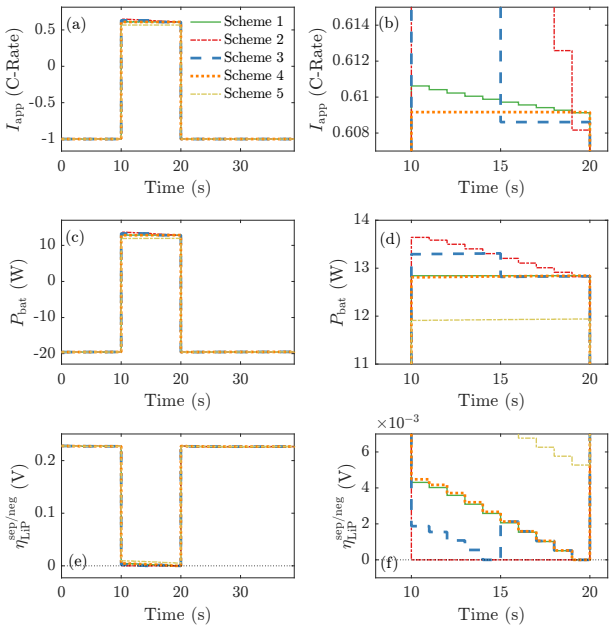

Fig. 4. Simulated results with different power capability estimation algorithms: (a) Current rate. (b) Current rate (detail). (c) Battery power. (d) Battery power (detail). (e) Li plating potential at the sep/neg boundary. (f) Li plating potential at the sep/neg boundary (detail).

$N^{\text{pos}} = 10$, $N^{\text{sep}} = 5$, and $N^{\text{pos}} = 10$. The noise-corrupted measurements $z(k)$ sampled at $\Delta t = 1$ s, were used for estimating the battery state $\hat{\mathbf{x}}(k)$ based on the ensemble-based estimator (25)–(31). The constraints were selected as $\overline{I}_{\text{app}} = 4\text{C}$, $\underline{I}_{\text{app}} = -4\text{C}$, $\overline{V}_{\text{bat}} = 4.2$ V, $\underline{V}_{\text{bat}} = 2.5$ V, $\overline{P}_{\text{bat}} = 65$ W, $\underline{P}_{\text{bat}} = -65$ W, $\overline{\text{SOC}} = 1$, $\underline{\text{SOC}} = 0$, $\bar{c}_s^{\text{neg}} = 33,000$ mol/m^3, $\underline{c}_s^{\text{neg}} = 1000$ mol/m^3 , $\underline{c}_e = 200$ mol/m^3, $\underline{\eta}_{\text{LiP}} = 0$, and $\overline{T}_{\text{bat}} = 310.15$ K (37 °C). The constrained nonlinear optimization problems (16) and (18) were solved using `fmincon` function with the sequential quadratic programming.

B. Comparison of Different Physics-Based Models

In order to demonstrate why and how the proposed algorithm based on a high-dimensional physics-based model is superior to existing electrochemical models for power capability prediction, we first compare the predicted power capability with 1) a single particle model enhanced by electrolyte and thermal dynamics (SPM-eT) [22] and 2) a single particle model with thermal dynamics (SPM-T) [23]. In both the SPM-eT and SPM-T, the distributed behaviors along the electrode thickness are ignored, and it is assumed that spatio-temporal variables such as the molar flux, solid-phase concentration, and overpotentials for reactions are all uniform in the respective electrode [1]. Note that in this example, the same model is used for both simulating the battery and power capability estimation. The battery is discharged at room temperature ($T_{\text{amb}} = 25$ °C) with 1C constant current from SOC = 0.9. Suppose the battery requires a 10-s charging power to achieve regenerative braking from 10 s to 20 s (i.e., $N_{\mathcal{J}} = 10$). The simulated results with the three PBMs are shown in Fig. 3. At this high SOC level, the limiting factor is the Li plating potential: As can be observed from Fig. 3(b), by applying the maximum charging power, all the local Li plating potentials can be kept nonnegative. However, the predicted power capabilities from different models have significant differences, as can be seen in Fig. 3(e) and Fig. 3(f). The reason for these differences is mainly because for a thick electrode, there are considerable nonuniform behaviors (see Fig. 3(c) and Fig. 3(d)). The resulting Li plating potential should be much lower in the neg/sep boundary than in other positions, and this can be accurately captured by the P2D-T model. In contrast, both the SPM-eT and SPM-T are only able to predict the average effects of the Li plating potential. Fig. 3(e) shows that the predicted charge power capabilities are overestimated for these ROMs. For a real battery, overestimated power capability can lead to aggressive control and accelerated aging/failure. Hence, the results demonstrate the significance of using the high-dimensional model for predicting the battery power capability to consider battery health information.

C. Comparison of Different Power Capability Prediction Algorithms

Under the same operating condition as the previous subsection, we evaluate the effectiveness of different algorithms to predict the battery power capability. In this case, the true battery state is assumed to be accessible, and thus the state estimator is not applied. Five schemes are compared, including

1) Global optimization for Problem 1 (benchmark);
2) Algorithm 1.1 with $N_{\mathcal{L}} = 1, H = 1, N_O = 10$;
3) Algorithm 1.2 with $N_{\mathcal{L}} = 5, H = 5, N_O = 2$; and

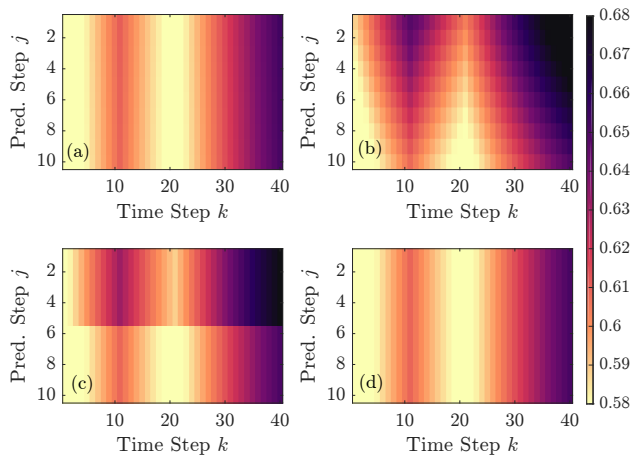

Fig. 5. Colormap of the calculated current sequence $\mathbf{u}_+^\star(k)$ in the units of C-rate, $1 \le k \le 40$. (a)–(d) Schemes 1–4.

4) Algorithm 1.2 with $N_\mathcal{L} = 10, H = 10, N_O = 1$.
5) LTV-MPC with $N_\mathcal{L} = 10, H = 10, N_O = 1$.

The results are shown in Fig. 4 and Fig. 5, and the performances are summarized in Table I. In this case, according to Scheme 1, the true charge power capability at $t = 10$ s is 12.84 W. From Figs. 4(e) and (f), the Li plating potential η_{LiP} are all maintained nonnegative to avoid accelerated battery aging. For Algorithm 1.1 (Scheme 2), both power and current are reduced in a drastic manner due to its shortsightedness during prediction. The predicted power at the end of the period is slightly lower than the benchmark value. However, Scheme 2 demands high computation, as indicated in Table I. In contrast, we consider that Algorithm 1.2 (Schemes 3 and 4) has the advantages of high accuracy and computational efficiency. However, Fig. 4(d) shows that for Scheme 4, the last element in the sequence is slightly higher than the benchmark value, which might lead to the violation of the constraints. Hence, Scheme 3 will be used to demonstrate the performance of the proposed power capability estimation method next, as its conservativeness can offer a certain safety margin. Furthermore, the results of the LTV-MPC-based algorithm (Scheme 5) show that the estimated charge power capability is underestimated due to the overestimated Li plating potential. The predicted charge power capability is about 7% lower than the benchmark value. Although from Figs. 4(e) and (f), the LTV-MPC scheme is seen to provide a 0.005-V safety margin against Li plating, whether such a good property is available under all operating conditions and with different battery parameters need further investigation.

TABLE I
COMPARISON OF PERFORMANCES OF DIFFERENT SCHEMES

Scheme	1	2	3	4	5
P_{bat} (W) at $t = 20$ s	12.84	12.82	12.83	12.85	11.95
CPU runtime (s)	25.1	1.0	0.26	0.22	0.02

Fig. 6 shows the results under alternate charge and discharge current pulses according to the predicted maximum power,

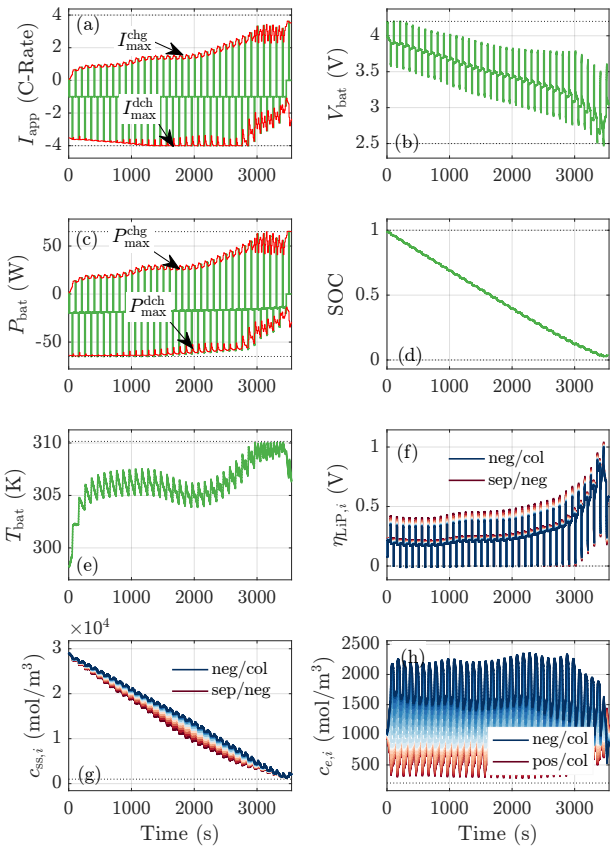

Fig. 6. Power capability evaluation under pulse conditions. (a) Applied current and power capability in terms of C-rates. (b) Terminal voltage. (c) Terminal power and power capabilities. (d) SOC. (e) Battery temperature. (f) Lithium plating potential in the negative electrode. (g) Solid-phase surface concentration in the negative electrode (h) Electrolyte concentration. The dotted lines are respective operating limits.

superimposed on a constant 1C discharge profile. From the high to the low SOC levels, it can be seen that the successive limits of the charge power capability are the voltage, Li plating potential, temperature, and power rating. On the other hand, the discharge power capability is sequentially limited by the power rating, current, temperature, and solid-phase concentration. Furthermore, it is also shown that the electrolyte concentration and SOC are not limiting factors for the power capability. This example exhibits the significance of considering the electrochemical and thermal quantities as constraints for power capability calculation.

D. Power Capability Estimation Under a Dynamic Profile

By incorporating the EnKF-based battery state estimator in Section IV-C, Fig. 7 shows the charge power capability estimation results based on the proposed algorithm under a modified Federal Urban Dynamic Schedule (FUDS) profile with the initial SOC being 0.99. The ensemble size is chosen to be $N_\mathcal{P} = 5$, and the measurement covariance is $\mathbf{R} = (0.01\ \text{V})^2$. The amplitude of the original current profile is doubled, leading to a maximum current rate of 3C. We compare the proposed method with a conventional scheme where only battery current, voltage, and terminal power are

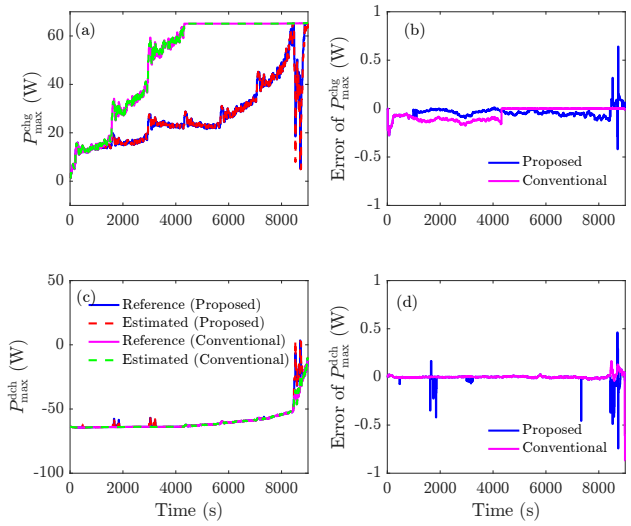

Fig. 7. Power capability estimation under a modified FUDS profile (a) Reference and estimated charge power capability. (b) Estimation errors of charge power capability. (c) Reference and estimated discharge power capability. The legend is the same as Fig. 7(a). (d) Estimation errors of discharge power capability.

considered as constraints. Since no internal electrochemical-thermal variables are considered in this conventional scheme, an ECM can be used with a similar NMPC algorithm proposed in the present work. It can be seen from Fig. 7(a) that the allowable maximum charge power is much lower than the one only limited by the external electrical constraint after about 1100 s. This reduced charging capability is mainly limited by the internal constraints on Li plating and temperature. On the other hand, as can be observed from Fig. 7(c), a considerably reduced discharge power capability can be seen at the end of the cycling process where the temperature limit has been reached.

Based on the proposed scheme, the root-mean-square error (RMSE) and maximum absolute error (MAE) of the charging power capability estimation are 0.08% and 0.98%, respectively. The RMSE and MAE of the discharging power estimation are 0.02% and 1.14%, respectively. These results highlight the high accuracy of the proposed power capability estimation scheme. It should also be mentioned that as shown in Fig. 8, it requires an average of 0.15 s for the CPU to calculate the charge and discharge power capabilities per sampling time ($\Delta t = 1$ s), and 95% CPU runtime is shorter than 0.2 s. Thus, the computational load of the proposed algorithm is considered affordable for online operation.

In another example shown in Fig. 9, we compare the results of the estimated power capabilities under the different ambient temperatures. In this example, the upper temperature limit was raised up to $T_{\text{amb}} = 45$ °C. It can be readily observed from Figs. 9(a) and (b) that at zero ambient temperature, both the charging and discharging capabilities would be significantly reduced compared to the case under the standard temperature condition of 25 °C. In the low-temperature environment ($T_{\text{amb}} = 0$ °C), the charging and discharging capabilities are mainly limited by the terminal voltage, Li plating potential at the sep/neg boundary, and the concentration at the pos/col

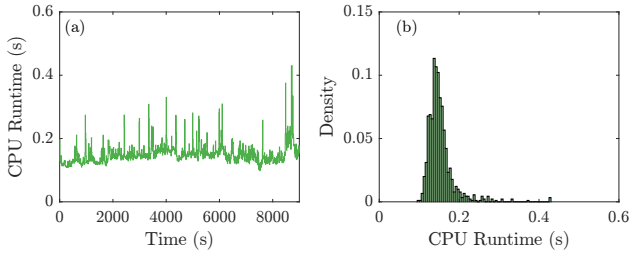

Fig. 8. Computational efficiency in terms of (a) average CPU runtime per sample and (b) distribution of CPU runtime.

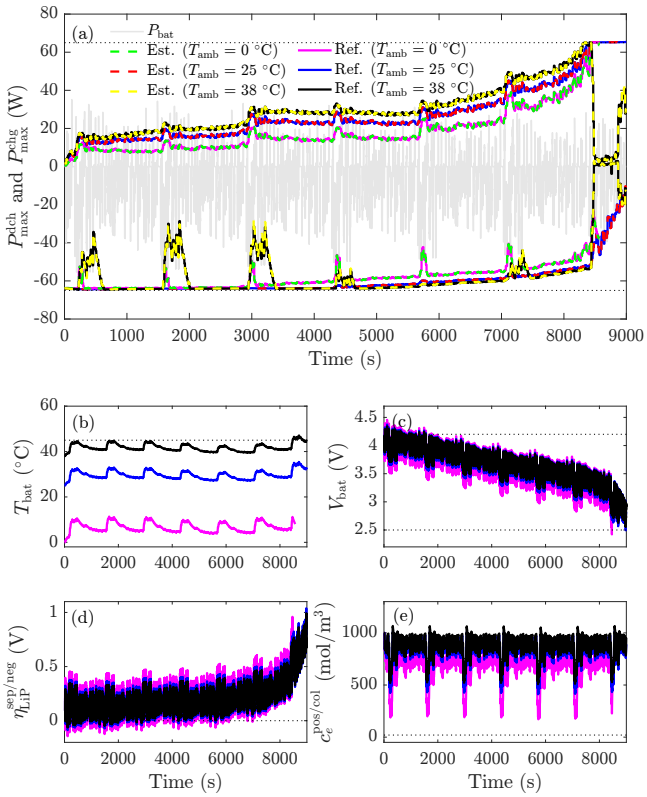

Fig. 9. Impact of temperature on the power capability of Li-ion batteries under a modified FUDS current profile. (a) Battery power and power capability estimation result. (b) Battery temperature. (c) Terminal voltage. (d) Li plating potential at the sep/neg boundary. (e) Electrolyte concentration at the pos/col boundary.

boundary, respectively, which can be shown from Figs. 9(c)–(e). On the other hand, under a high ambient temperature ($T_{\text{amb}} = 38$ °C), the charge power capability is generally increased. However, the discharge power might be reduced during the period when the battery temperature is close to the upper limit, as can be observed from Fig. 9(c). Within this wide temperature range, the proposed algorithm can achieve high estimation accuracy in the power capability with an average RMSE of less than 0.1%.

VI. Conclusion

We propose a framework of power capability estimation for lithium-ion batteries. Compared to the existing method, we use a high-fidelity electrochemical-thermal model to predict the battery's internal behaviors that can limit the operation of the

TABLE II
ELECTROCHEMICAL-THERMAL PARAMETERS IN THE P2D-T MODEL

Symbol	Unit	$i \in \mathcal{I}^{\text{pos}}$	$i \in \mathcal{I}^{\text{sep}}$	$i \in \mathcal{I}^{\text{neg}}$
R_p	m	$5.22 \cdot 10^{-6}$	–	$5.86 \cdot 10^{-6}$
D_s	m^2/s	$4.0 \cdot 10^{-15}$	–	$3.3 \cdot 10^{-14}$
ε_s	–	0.665	–	0.75
a_s	m^2/s	382, 183	–	383, 959
$c_{s,0\%}$	mol/m^3	52, 782	–	856
$c_{s,100\%}$	mol/m^3	16, 650	–	29, 283
$c_{s,\max}$	mol/m^3	63, 104	–	33, 133
σ	S/m	0.18	–	215
k	$\text{A} \cdot \text{m}^{2.5}/\text{mol}^{1.5}$	$3.5 \cdot 10^{-11}$	–	$6.7 \cdot 10^{-12}$
r_f	$\Omega \cdot \text{m}^2$	0	–	0.01
E_a^{ϕ}	J	17, 800	–	35, 000
E_a^{De}, E_a^{κ}	J	20, 000 *	20, 000 *	20, 000 *
δ	m	$75.6 \cdot 10^{-6}$	$12 \cdot 10^{-5}$	$85.2 \cdot 10^{-6}$
ε_e	–	0.335	0.47	0.25
brugg	–		1.5	
$\mathcal{R}$	$\text{J}/(\text{K} \cdot \text{mol})$		8.314	
$\mathcal{F}$	C/mol		96, 487	
A	m^2		0.1027	
T_{ref}	K		298.15	
T_{amb}	K		298.15	
c_e^0	mol/m^3		1000	
t_a^0	–		0.7406	
R_{col}	Ω		0.001 *	
C_T	J/K		17.79 *	
R_T	K/W		8.43 *	

*: Assumed

TABLE III
CONCENTRATION/TEMPERATURE-DEPENDENT FUNCTIONS IN THE P2D-T MODEL

1) Effective electrolyte diffusion coefficient (m^2/s):

$$D_{e,i} = \varepsilon_{e,i}^{\text{brugg}} \cdot [8.794 \times 10^{-11} \cdot (c_{e,i}/1000)^2 - 3.972 \times 10^{-10} \cdot (c_{e,i}/1000) + 4.862 \times 10^{-10}]$$

2) Effective electrolyte conductivity (S/m) [14]:

$$\kappa_i = \varepsilon_{e,i}^{\text{brugg}} \cdot [0.1297 \cdot (c_{e,i}/1000)^3 - 2.51 \cdot (c_{e,i}/1000)^{1.5} + 3.329 \cdot (c_{e,i}/1000)]$$

3) The OCP function is expressed by

$$f_{\text{ss},i}(c_{\text{ss},i}, T_{\text{bat}}) = U_{\text{ref},i} + (\partial U/\partial T)_i (T_{\text{bat}} - T_{\text{ref}})$$

For the positive electrode ($i \in \mathcal{I}^{\text{pos}}, \theta := c_{\text{ss},i}/c_{s,\max,i}$)

$$\begin{aligned} U_{\text{ref},i} = &-0.8090\theta + 4.4875 - \\ &0.0428 \tanh(18.5138(\theta - 0.5542)) - \\ &17.7326 \tanh(15.7890(\theta - 0.3117)) + \\ &17.5842 \tanh(15.9308(\theta - 0.3120)) \end{aligned}$$

For the negative electrode ($i \in \mathcal{I}^{\text{neg}}, \theta := c_{\text{ss},i}/c_{s,\max,i}$)

$$\begin{aligned} U_{\text{ref},i} = &1.97938 \exp(-39.3631\theta) + 0.2482 - \\ &0.0909 \tanh(29.8538(\theta - 0.1234)) - \\ &0.04478 \tanh(14.9159(\theta - 0.2769)) - \\ &0.0205 \tanh(30.4444(\theta - 0.6103)) \end{aligned}$$

Entropy coefficients $(\partial U/\partial T)_i$: Positive electrode [24]; Negative electrode [14]

4) Electrolyte: $U_{e,i} = f_{e,i} = (c_{e,i}, T_{\text{bat}}) = \frac{2\mathcal{R}T_{\text{bat}}t_a^0}{\mathcal{F}} \ln\left(\frac{c_{e,i}}{c_e^0}\right)$

5) Resistances (Ω):

$$\begin{aligned} R_{e,i+0.5} &= (\Delta\delta_i/\kappa_i^{\text{eff}} + \Delta\delta_{i+1}/\kappa_{i+1}^{\text{eff}})/(2A) \\ R_{s,i+0.5} &= (\Delta\delta_i/\sigma_i^{\text{eff}} + \Delta\delta_{i+1}/\sigma_{i+1}^{\text{eff}})/(2A) \\ R_e^{\text{sep}} &= \sum\nolimits_{i=N^{\text{pos}}}^{N^{\text{pos}}+N^{\text{sep}}} R_{e,i+0.5} \\ R_{\Sigma,i} &= (r_{\text{ct},i} + r_{f,i}^{\text{eff}})/(A\Delta\delta_i a_{s,i}) \\ r_{\text{ct},i} &= \mathcal{R}T_{\text{bat}}/[\mathcal{F}^2 k_i^{\text{eff}} \sqrt{c_{e,i} c_{\text{ss},i}(c_{s,\max,i} - c_{\text{ss},i})}] \end{aligned}$$

6) Temperature-dependent parameters (Arrhenius equation):

$$\phi_i^{\text{eff}} = \phi_i \exp\left(-\frac{E_{a,i}^{\phi}}{\mathcal{R}}\left(\frac{1}{T_{\text{bat}}} - \frac{1}{T_{\text{ref}}}\right)\right), \quad \phi \in \{k, D_s, \sigma, r_f, D_e, \kappa\}$$

Note: brugg is the Bruggeman's constant, $\mathcal{R}$ is the universal gas constant, T_{ref} is the reference temperature, and c_e^0 is the average electrolyte concentration.

battery under extreme conditions with wide temperature ranges and high current rates. Conventionally, these operating modes are avoided due to the lack of a pathway to design a health- and safety-aware algorithm. With the highly accurate but more complex model, formulating the power capability estimation into an optimal control problem requires tractable algorithms for real-time operation. To prevent the loss of model fidelity, we reduce the global optimization problem into a finite-time nonlinear optimization problem and solve it using multistep NMPC. The algorithm is aided by precise battery internal state information estimated using an ensemble-based estimator. Comparative studies have shown that the proposed method is effective in estimating the power capability under a wide operating range by considering additional electrochemical and thermal constraints that cannot be imposed in conventional methods. The presented framework can be extended by incorporating additional constraints and/or control objectives, such as those related to other degradation modes and nonuniform temperature distribution, once mathematical descriptions of respective physical mechanisms are available. However, as the predictive model becomes more complex, additional investigations on model reduction are essential to further improve the computational efficiency for low-cost implementation.

APPENDIX

A. Reduced-Order Diffusion Equations and Model Parameters

In the original P2D model, the diffusion of Li species in the solid phase is governed by a two-scale PDE for each electrode. We first apply the FVM on the macroscale and then use a frequency-domain method [25] on the particle scale to reduce the PDE into an ODE submodel, i.e., $\forall i \in \mathcal{I}^{\text{pos}} \cup \mathcal{I}^{\text{neg}}, \forall m \in \{1, 2, \cdots, M\}$,

$$\dot{\tilde{c}}_{s,i,m} = -\frac{\alpha_m D_{s,i}^{\text{eff}}}{R_{p,i}^2}\tilde{c}_{s,i,m} - \frac{\beta_m}{R_{p,i}}\frac{I_{n,i}}{\mathcal{F}A\Delta\delta_i a_{s,i}} \tag{A1}$$

$$c_{\text{ss},i} = \sum_{m=1}^{M} \tilde{c}_{s,i,m} \tag{A2}$$

$$c_{s,\text{avg}}^{\text{neg}} = \sum_{i \in \mathcal{I}^{\text{neg}}} \tilde{c}_{s,i,m=1} \tag{A3}$$

where $D_{s,i}^{\text{eff}}$ is the effective solid-phase diffusion coefficient, $R_{p,i}$ is the particle radius, $\mathcal{F}$ is the Faraday constant, A is the electrode cross-sectional area, $a_{s,i}$ is the solid-phase surface area per electrode volume, and $\Delta\delta_i$ is the width of the control volume. α_m and β_m are dimensionless coefficients determined

by the selected system order M of the submodel. We adopt $M = 2$ in this work, which gives $\alpha_1 = 0, \beta_1 = 3, \alpha_2 = 35$, and $\beta_2 = 7$.

On the other hand, the ODE that governs the dynamics of the electrolyte concentration is obtained by applying the FVM to the corresponding PDE in the original P2D model, i.e.,

$$\dot{c}_{e,i} = \frac{1}{\Delta\delta_i \varepsilon_{e,i}} \left(\frac{D^{\text{eff}}_{e,i+0.5}}{0.5} \frac{c_{e,i+1} - c_{e,i}}{\Delta\delta_{i+1} + \Delta\delta_i} - \frac{D^{\text{eff}}_{e,i-0.5}}{0.5} \frac{c_{e,i} - c_{e,i-1}}{\Delta\delta_{i-1} + \Delta\delta_i} \right) + \lambda_i, \tag{A4}$$

where $\lambda_i = \frac{t_a^0}{\varepsilon_{e,i}} \frac{I_{n,i}}{\mathcal{F} A \Delta\delta_i}, \forall i \in \mathcal{I}^{\text{pos}} \cup \mathcal{I}^{\text{neg}}$; $\lambda_i = 0, \forall i \in \mathcal{I}^{\text{sep}}$. $D^{\text{eff}}_{e,i\pm0.5} = (\Delta\delta_i + \Delta\delta_{i+1}) / \left(\Delta\delta_i / D^{\text{eff}}_{e,i} + \Delta\delta_{i\pm1} / D^{\text{eff}}_{e,i\pm1} \right)$. Here, $D^{\text{eff}}_{e,i}$ is the effective electrolyte diffusion coefficient, $\varepsilon_{e,i}$ is the porosity, and t_a^0 is the transference number.

The concentration state vector $\mathbf{x}_c$, and the matrices $\mathbf{A}_c$, $\mathbf{B}_c$, and $\mathbf{C}_c$ in (5) and (6) can be thus readily obtained but not explicitly provided here. The parameters used in this work are given in Table II and Table III, mainly obtained from [26] for a 5-Ah NMC 811/graphite-silicon battery except where noted.

B. An Implicit-Explicit Method

First, Substituting (3) and (4) into (5) yields the dynamic equation for the concentrations of the form

$$\dot{\mathbf{x}}_c = \mathbf{A}_c \mathbf{x}_c + \mathbf{B}_1 u + \mathbf{B}_2 \tag{B1}$$

where $\mathbf{A}_c$, $\mathbf{B}_1$, and $\mathbf{B}_2$ are matrices depending on the state $\mathbf{x} = [\mathbf{x}_c^\top, T_{\text{bat}}]^\top$. We discretize (B1) as

$$[\mathbf{x}_c(k+1) - \mathbf{x}_c(k)]/\Delta t = \mathbf{A}_c \mathbf{x}_c(k+1) + \mathbf{B}_1 u(k) + \mathbf{B}_2 \tag{B2}$$

where k is the discrete time instant and Δt is the sampling time. Solving (B2) yields

$$\mathbf{x}_c(k+1) = (\mathbf{I} - \Delta t \mathbf{A}_c)^{-1} (\mathbf{x}_c(k) + \Delta t \mathbf{B}_1 u(k) + \Delta t \mathbf{B}_2) \tag{B3}$$

where $\mathbf{I}$ is the identity matrix, and matrices $\mathbf{A}_c$, $\mathbf{B}_1$, and $\mathbf{B}_2$ are calculated based on $\mathbf{x}(k)$.

This discretization method can also be applied to the temperature equation (8). We then obtain an explicit expression of the state transition equation in the form of (11).

REFERENCES

[1] Y. Li, D. Karunathilake, D. M. Vilathgamuwa, Y. Mishra, T. W. Farrell, S. S. Choi, and C. Zou, "Model order reduction techniques for physics-based lithium-ion battery management: A survey," *IEEE Ind. Electron. Mag.*, vol. 16, no. 3, pp. 36–51, Sep. 2022.

[2] H. Rahimi-Eichi, U. Ojha, F. Baronti, and M. Chow, "Battery management system: An overview of its application in the smart grid and electric vehicles," *IEEE Ind. Electron. Mag.*, vol. 7, no. 2, pp. 4–16, Jun. 2013.

[3] G. L. Plett, "High-performance battery-pack power estimation using a dynamic cell model," *IEEE Trans. Veh. Technol.*, vol. 53, no. 5, pp. 1586–1593, Sep. 2004.

[4] Q. Ouyang, Z. Wang, K. Liu, G. Xu, and Y. Li, "optimal charging control for lithium-ion battery packs: A distributed average tracking approach," *IEEE Trans. Ind. Informat.*, vol. 16, no. 5, pp. 3430–3438, 2020.

[5] X. Wang, J. Wang, and J. Liu, "Vehicle to grid frequency regulation capacity optimal scheduling for battery swapping station using deep Q-network," *IEEE Trans. Ind. Informat.*, vol. 17, no. 2, pp. 1342–1351, 2021.

[6] Y. Gao, X. Zhang, B. Guo, C. Zhu, J. Wiedemann, L. Wang, and J. Cao, "Health-aware multiobjective optimal charging strategy with coupled electrochemical-thermal-aging model for lithium-ion battery," *IEEE Trans. Ind. Informat.*, vol. 16, no. 5, pp. 3417–3429, 2020.

[7] W. Waag and D. U. Sauer, "Adaptive estimation of the electromotive force of the lithium-ion battery after current interruption for an accurate state-of-charge and capacity determination," *Appl. Energy*, vol. 111, pp. 416–427, Nov. 2013.

[8] R. Xiong, H. He, F. Sun, X. Liu, and Z. Liu, "Model-based state of charge and peak power capability joint estimation of lithium-ion battery in plug-in hybrid electric vehicles," *J. Power Sources*, vol. 229, pp. 159–169, May 2013.

[9] C. Zou, A. Klintberg, Z. Wei, B. Fridholm, T. Wik, and B. Egardt, "Power capability prediction for lithium-ion batteries using economic nonlinear model predictive control," *J. Power Sources*, vol. 396, pp. 580–589, Aug. 2018.

[10] Z. Wei, J. Zhao, R. Xiong, G. Dong, J. Pou, and K. J. Tseng, "Online estimation of power capacity with noise effect attenuation for lithium-ion battery," *IEEE Trans. Ind. Electron.*, vol. 66, no. 7, pp. 5724–5735, Jul. 2019.

[11] A. Farmann and D. U. Sauer, "A comprehensive review of on-board state-of-available-power prediction techniques for lithium-ion batteries in electric vehicles," *J. Power Sources*, vol. 29, pp. 123–237, 2016.

[12] Z. Wei, J. Zhao, C. Zou, T. M. Lim, and K. J. Tseng, "Comparative study of methods for integrated model identification and state of charge estimation of lithium-ion battery," *J. Power Sources*, vol. 402, pp. 189–197, Oct. 2018.

[13] K. A. Smith, C. D. Rahn, and C.-Y. Wang, "Model-based electrochemical estimation and constraint management for pulse operation of lithium ion batteries," *IEEE Trans. Control Syst. Technol.*, vol. 18, no. 3, pp. 654–663, May 2010.

[14] Y. Li, M. Vilathgamuwa, T. Farrell, S. S. Choi, N. T. Tran, and J. Teague, "A physics-based distributed-parameter equivalent circuit model for lithium-ion batteries," *Electrochimica Acta*, vol. 299, pp. 451–469, Mar. 2019.

[15] C. Zou, X. Hu, Z. Wei, T. Wik, and B. Egardt, "Electrochemical estimation and control for lithium-ion battery health-aware fast charging," *IEEE Trans. Ind. Electron.*, vol. 65, no. 8, pp. 6635–6645, Aug. 2018.

[16] L. Zheng, J. Zhu, G. Wang, D. D. Lu, and T. He, "Lithium-ion battery instantaneous available power prediction using surface lithium concentration of solid particles in a simplified electrochemical model," *IEEE Trans. Power Electron.*, vol. 33, no. 11, pp. 9551–9560, 2018.

[17] A. M. Boyce, D. J. Cumming, C. Huang, S. P. Zankowski, P. S. Grant, D. J. L. Brett, and P. R. Shearing, "Design of scalable, next-generation thick electrodes: Opportunities and challenges," *ACS Nano*, vol. 15, no. 12, pp. 18 624–18 632, Dec. 2021.

[18] X.-G. Yang, G. Zhang, S. Ge, and C.-Y. Wang, "Fast charging of lithium-ion batteries at all temperatures," *Proc. Nat. Acad. Sci.*, vol. 115, no. 28, p. 7266, 2018.

[19] S. Marelli and M. Corno, "Model-based estimation of lithium concentrations and temperature in batteries using soft-constrained dual unscented kalman filtering," *IEEE Trans. Control Syst. Technol.*, vol. 29, no. 2, pp. 926–933, Mar. 2021.

[20] Y. Li, B. Xiong, D. M. Vilathgamuwa, Z. Wei, C. Xie, and C. Zou, "Constrained ensemble Kalman filter for distributed electrochemical state estimation of lithium-ion batteries," *IEEE Trans. Ind. Inform.*, vol. 17, no. 1, pp. 240–250, Jan. 2021.

[21] Y. Li, Z. Wei, B. Xiong, and D. M. Vilathgamuwa, "Adaptive ensemble-based electrochemical-thermal degradation state estimation of lithium-ion batteries," *IEEE Trans. Ind. Electron.*, vol. 69, no. 7, pp. 6984–6996, Jul. 2022.

[22] H. E. Perez, X. Hu, and S. J. Moura, "Optimal charging of batteries via a single particle model with electrolyte and thermal dynamics," in *Proc. Amer. Control Conf.*, 6-8 Jul. 2016, pp. 4000–4005.

[23] M. Guo, G. Sikha, and R. E. White, "Single-particle model for a lithium-ion cell: Thermal behavior," *J. Electrochem. Soc.*, vol. 158, no. 2, pp. A122–A132, 2011.

[24] A. Eddahech, O. Briat, and J.-M. Vinassa, "Thermal characterization of a high-power lithium-ion battery: Potentiometric and calorimetric measurement of entropy changes," *Energy*, vol. 61, pp. 432–439, Nov. 2013.

[25] Y. Li, T. Wik, C. Xie, Y. Huang, B. Xiong, J. Tang, and C. Zou, "Control-oriented modeling of all-solid-state batteries using physics-

based equivalent circuits," *IEEE Trans. Transport. Electrific.*, vol. 8, no. 2, pp. 2080–2092, Aug. 2022.

[26] C.-H. Chen, F. Brosa Planella, K. O'Regan, D. Gastol, W. D. Widanage, and E. Kendrick, "Development of experimental techniques for parameterization of multi-scale lithium-ion battery models," *J. Electrochem. Soc.*, vol. 167, no. 8, p. 080534, Jan. 2020.

Yang Li (Member, IEEE) received the B.E. degree in electrical engineering from Wuhan University, Wuhan, China, in 2007, and the M.Sc. and Ph.D. degrees in power engineering from Nanyang Technological University (NTU), Singapore, in 2008 and 2015, respectively. He was a Research Fellow with the Energy Research Institute, NTU and the School of Electrical Engineering and Computer Science, Queensland University of Technology, Brisbane, QLD, Australia. Since 2019, he has been an faculty member with the School of Automation, Wuhan University of Technology, Wuhan. Since 2020, he has been a researcher with the Department of Electrical Engineering, Chalmers University of Technology, Gothenburg, Sweden. His research interests include modeling and control of energy storage systems in power grid and transport sectors.

Dr. Li is a recipient of the EU Marie Skłodowska-Curie Action Individual Fellowship in 2020. He serves as an Associate Editor for IEEE TRANSACTIONS ON INDUSTRIAL ELECTRONICS and IEEE TRANSACTIONS ON TRANSPORTATION ELECTRIFICATION.

Zhongbao Wei (Senior Member, IEEE) received the B.Eng. and M.Sc. degrees in instrumental science and technology from Beihang University. Beijing, China, in 2010 and 2013, respectively, and the Ph.D. degree in power engineering from Nanyang Technological University, Singapore, in 2017.

He was a Research Fellow with the Energy Research Institute, Nanyang Technological University, from 2016 to 2018. He is currently a Professor of vehicle engineering with National Engineering Laboratory for Electric Vehicles, School of Mechanical Engineering, Beijing Institute of Technology, Beijing. His research interests include battery modeling, identification, state estimation, diagnostic, and thermal management, with applications to renewable energy systems such as lithium-ion battery and vanadium redox flow battery.

Dr. Wei serves as an Associate Editor for many international journals like IEEE TRANSACTIONS ON INDUSTRIAL ELECTRONICS, IEEE TRANSACTIONS ON INTELLIGENT TRANSPORTATION SYSTEMS, and *IET Intelligent Transport Systems*.

Changjun Xie (Member, IEEE) received the Ph.D. degree in vehicle engineering from the Wuhan University of Technology (WUT), Wuhan, Hubei, China, in 2009. From 2012 to 2013, he was a Visiting Scholar with the University of California, Davis, California, USA. He is currently a Professor with the School of Automation, WUT, Wuhan, China. He is the Dean of Modern Industry College of Artificial Intelligence and New Energy Vehicles and the Director of the Institute of New Energy Detection and Control Technology, WUT. His research interests include battery management, control, and optimization of new energy vehicles.

D. Mahinda Vilathgamuwa (Fellow, IEEE) received the B.Sc. degree from the University of Moratuwa, Sri Lanka, in 1985, and the Ph.D. degree from Cambridge University, Cambridge, U.K., in 1993, both in electrical engineering.

In 1993, he joined the School of Electrical and Electronic Engineering, Nanyang Technological University, Singapore, where he had been a Faculty Member until 2013. He is currently a Professor of power engineering with Queensland University of Technology, Brisbane, Australia. His research interests include wireless power, battery storage, power electronic converters, electrical drives, and electromobility.